JOURNAL OF GEOPHYSICAL RESEARCH, VOL. 114, D11101, doi:10.1029/2008JD010112, 2009

Gravity wave propagation and dissipation from the stratosphere to the lower thermosphere

Xian Lu,[1] Alan Z. Liu,[2] Gary R. Swenson,[2] Tao Li,[3] Thierry Leblanc,[4] and I. Stuart McDermid[4]

Received 13 March 2008; revised 16 March 2009; accepted 30 March 2009; published 2 June 2009.

[1] One-night (28 October 2003) temperature and horizontal wind measurements by a resonance sodium (Na) wind/temperature lidar at Maui (20.7°N, 156.3°W) and temperature measurement by a Rayleigh lidar at Mauna Loa Observatory (MLO, 19.5°N, 155.6°W), Hawaii, were used to study gravity wave (GW) propagation from the lower stratosphere to the lower thermosphere. A dominant wave mode was identified from 35 to 103 km. The wave was partially dissipated and propagating upward with a scale height of temperature amplitude at ~14 km. A damping layer was present around the stratopause where the wave amplitude was small, which also corresponded to a low static stability layer. The vertical wavelengths were larger in the mesosphere (12–13 km) than in the stratosphere (6–7 km), consistent with the decreasing static stability with altitude. Hodograph analysis of the Na lidar wind data showed that the wave was propagating northward and the horizontal wavelength was 2140 km and intrinsic period was 15 h in the region 84–103 km. The apparent period was ~6 h and consistent with Doppler shift of the background wind. It is suggested that the convective zone over the equator to the south of Hawaii provided a constant GW source that is responsible for the observed GW throughout the night.

Citation: Lu, X., A. Z. Liu, G. R. Swenson, T. Li, T. Leblanc, and I. S. McDermid (2009), Gravity wave propagation and dissipation from the stratosphere to the lower thermosphere, *J. Geophys. Res.*, *114*, D11101, doi:10.1029/2008JD010112.

1. Introduction

[2] Atmospheric gravity waves (GWs) play important roles in transporting energy and momentum, influencing the mean circulation, thermal structure and variability of the mesosphere and lower thermosphere (MLT) region [*Fritts and Alexander*, 2003]. The most significant triggering forces for GWs in the lower atmosphere include topography, convection, wind shear, frontal systems, etc. Dissipation of GWs mainly results from wave breaking and instabilities [*Lindzen*, 1981; *Fritts and Rastogi*, 1985; *Fritts and Yuan*, 1989; *Lombard and Riley*, 1996; *Gardner et al.*, 2002; *Liu et al.*, 2004; *Li et al.*, 2005a, 2005b], wave-wave and wave-mean flow interactions [*Yeh and Liu*, 1981; *Fritts*, 1985], and radiative damping [*Bühler and McIntyre*, 1999]. Many observations and wave models have contributed greatly to the understanding of GW sources and their dissipation mechanisms.

[3] Observations of GW characteristics such as wave spectra, intrinsic properties, scales and magnitudes are essential to understanding GW momentum fluxes, instability dynamics and vertical constituents transport [*Swenson et al.*, 2003; *Liu and Gardner*, 2004, 2005]. GWs in the upper mesosphere have been frequently observed by Na resonance lidars [*Lintelman and Gardner*, 1994; *Hu et al.*, 2002; *Li et al.*, 2007], potassium resonance lidars [*Fricke-Begemann et al.*, 2002; *Friedman*, 2003], radars [*Manson and Meek*, 1988; *Gavrilov et al.*, 1996; *Serafimovich et al.*, 2005] and airglow imagers [*Taylor et al.*, 1995; *Smith et al.*, 2000; *Tang et al.*, 2002; *Li et al.*, 2005b]. Observations in the stratosphere and lower mesosphere are often made using Rayleigh lidar technique [*Chanin and Hauchecorne*, 1981; *Gardner et al.*, 1989; *Whiteway and Carswell*, 1995; *Murayama et al.*, 1994; *Sivakumar et al.*, 2006]. Combining Rayleigh lidar and resonance lidar can provide simultaneous measurement of GWs from stratosphere to the mesopause, enabling study of their propagations from lower atmosphere to the MLT region. Such simultaneous measurements [*Dao et al.*, 1995; *She et al.*, 1995; *Alpers et al.*, 2004; *Rauthe et al.*, 2006] are not very common and simultaneous lidar observation of GW activities in low latitudes has not yet been reported. In this paper, we carried out a case study of observed gravity waves at low latitude using temperature measurements from Rayleigh lidar and temperature/wind measurements from Na lidar on Hawaii islands (~20°N). In 2003, both lidars made temperature measurements and had a decent overlapping observation period on the night of 28 October. On this particular night, temperature/wind measurements from Na lidar have been used to study the dynamical instabilities by *Li et al.* [2005b]. In this paper, we combined the Na and Rayleigh lidar measurements on this

[1]Department of Atmospheric Sciences, University of Illinois at Urbana-Champaign, Urbana, Illinois, USA.
[2]Department of Electrical and Computer Engineering, University of Illinois at Urbana-Champaign, Urbana, Illinois, USA.
[3]School of Earth and Space Sciences, University of Science and Technology of China, Hefei, China.
[4]Table Mountain Facility, Jet Propulsion Laboratory, California Institute of Technology, Wrightwood, California, USA.

0148-0227/09/2008JD010112$09.00

night and used them to study GW wave propagation and dissipation in the stratosphere and mesosphere.

2. Data and Analysis Methods

2.1. Data

[4] The JPL Rayleigh/Raman lidar at Mauna Loa Observatory (MLO, 19.5°N, 155.6°W) has been making regular measurements of ozone, temperature and aerosol profiles for the Network for Detection of Stratospheric Change (NDSC) program since July 1993 [*McDermid et al.*, 1995]. The current system of JPL Rayleigh/Raman lidar at MLO employs a Nd:YAG laser emitting at 355 nm, a 1-m Cassegrain telescope collecting the laser light backscattered by the atmospheric molecules, and a set of beam splitters dividing the collected signals into three temperature-dedicated channels. Two of these channels receive elastic Rayleigh/Mie-backscattered light at 355 nm for the retrieval of temperature between ~30 and 90 km, and one receives Raman-shifted light backscattered by atmospheric nitrogen at 387 nm, which allows temperature retrieval from 40 km down to about 15 km even in the presence of thin volcanic aerosols and clouds. A detailed description is given by *Leblanc et al.* [1999a, 1999b]. The raw signals were initially collected in 300-m vertical bins and saved every 4–10 min. Depending on the signal-to-noise ratio of the data and the nature of application, the analysis programs further average the raw photon profiles over a longer time interval and over a larger vertical range. In the raw data analysis, the raw photon profiles were smoothed with a hamming window function (2 km is the full width half maximum). The number of photons is proportional to the air density and temperature is then derived according to the hydrostatic balance approximation. The selected reference point is dependent on the signal-to-noise ratio and usually between 80 and 90 km. The reference temperature comes from MSIS-90 model. The 15 K difference between the reference atmosphere and the real temperature is common at the top of the profile. The uncertainty due to this temperature difference decreases when integrating the profile downward, reaching about only 3 K at 80 km and less than 1 K near 75 km [*Leblanc et al.*, 1998]. Therefore, the temperature uncertainty we derived below 80 km is mainly due to the photon noise. The relative uncertainty of temperature is inversely proportional to the square root of received photon counts. As the altitude increases, received photons decrease exponentially with the altitude, and temperature errors increase rapidly. The JPL system at MLO was upgraded in early 2001, leading to more output power at 355 nm (~10 W), and higher signal-to-noise ratio of return signals in the stratosphere and mesosphere [*Li et al.*, 2008].

[5] The University of Illinois (UIUC) Na wind/temperature lidar system [*Gardner and Papen*, 1995] measured the temperature from ~80 to 105 km. The UIUC Na wind/temperature lidar system was located on Mt. Haleakala in Maui, HI (20.7°N, 156.3°W), which is ~150 km away from MLO. The lidar system was coupled with a steerable 3.67 m diameter astronomical telescope at the Air Force Maui Optical Station. It has made high-resolution measurements of Na density, temperature, and winds in 35 nights during the period from January 2002 to March 2005. The temporal resolution of the temperature measurement is ~2 min and vertical resolution is 480 m. The lidar was directed to the zenith (Z), 30° off zenith toward north (N), east (E), south (S) and West (W) in the sequence of ZNEZSW. Horizontal winds were calculated by using off-zenith line-of-sight winds. For this night, the Rayleigh lidar observation started from 0501 to 1513 UT and Na lidar started from 0519 to 1555 UT. The overlapping observation period between 0519 and 1513 UT was selected for the study. The Na lidar data were smoothed temporally by using a 12-min Hanning window to obtain the same temporal resolution as the Rayleigh lidar data. At this resolution, the minimum nightly averaged uncertainty of temperature for Na lidar is ~0.5 K at 92.3 km and increases to ~1.5 K below 84 km and ~3.5 K above 103 km. Therefore only the observations between 84 and 103 km were used.

[6] In this paper, relative temperature perturbations were used to study wave propagation and dissipation by investigating their spectral behaviors and vertical variations of temperature perturbations. Wind perturbations from Na lidar were also used to derive wave properties, such as horizontal wavelength, propagation direction as well as intrinsic period. Both temperature and wind perturbations were derived by subtracting the nightly mean series and relative temperature perturbations were calculated by dividing the temperature perturbations by the nightly mean. Since the influences of diurnal and semidiurnal tides are not negligible in low latitudes like Mauna Loa and Maui, the perturbation at each altitude was detrended by fitting and subtracting a second-order polynomial as a function of time in order to minimize the tidal effects. By subtracting this background, contributions from low-frequency waves were effectively reduced if not removed. A linear trend of each vertical profile was also removed to reduce the effects of long vertical wavelength waves.

[7] Both Rayleigh and Na temperature perturbations were interpolated to the same vertical interval of 0.5 km. Since the raw data of Rayleigh temperature were smoothed with full-width-half-maximum (FWHM) of 2 km, waves with vertical wavelengths less than 2 km were removed. Therefore the data used in this study can be used to identify GWs with vertical wavelengths longer than 2 km and wave periods longer than 24 min.

2.2. Analysis Methods

[8] Hodograph method was used to derive GW intrinsic properties from Na lidar temperature and wind similar to *Hu et al.* [2002]. After wind and temperature perturbations were derived, we used Welch's averaged periodogram spectral estimation method [*Welch*, 1967] to obtain the average dominant vertical wave number. For every vertical profile, a dominant wave number is identified when there were peaks at common wave number on both temperature and wind spectra that exceed a confidence level. The average wave number (m_0) was then used in a GW model to fit the wind and temperature perturbations. The model consists of wave amplitudes (u_0, v_0, T_0), an exponential term, and a sinusoidal component. The GW model is described as:

$$\begin{aligned} u'(z) &= u_0 \exp(\beta z)\cos(m_0 z + \theta_u), \\ v'(z) &= v_0 \exp(\beta z)\cos(m_0 z + \theta_v), \\ T'(z) &= T_0 \exp(\beta z)\cos(m_0 z + \theta_T), \end{aligned} \tag{1}$$

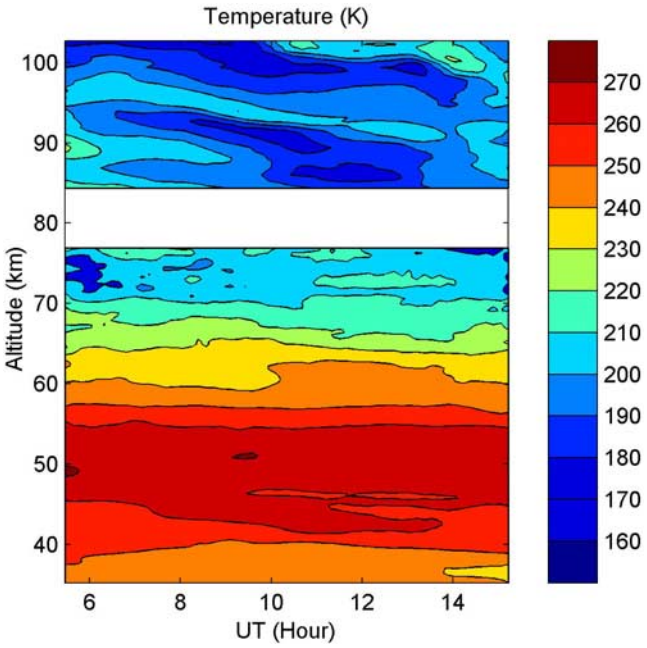

Figure 1. Temperature on the night of 28 October 2003. Data below 80 km are from Rayleigh lidar and above 80 km are from Na lidar. The gap around 80 km is where both Na lidar and Rayleigh lidars have low signals and no reliable temperature can be obtained.

where u' is the in-phase wind perturbation along the wave propagation direction, v' is the wind perturbation perpendicular to the wave propagation direction and T' is the temperature perturbation. The intrinsic frequency ω was then determined from the polarization relation:

$$|u'|/|v'| = \omega/f, \tag{2}$$

where f is the inertial frequency. The corresponding inertial period at the latitude of 20° is 35.1 h. The horizontal wave number k was determined from the dispersion relation [*Fritts and Alexander*, 2003],

$$k^2 = \frac{\omega^2 - f^2}{N_0^2} m_0^2, \tag{3}$$

where N_0 is the vertically averaged Brunt-Väisälä frequency. In the hodograph of zonal and meridional winds, the major axis determines the horizontal direction of wave propagation and the length ratio of the major to minor axes equals to the ratio of intrinsic to inertial frequencies. The details of the hodograph method is given by *Hu et al.* [2002].

[9] In order to investigate the variation of the dominate vertical wavelength with the altitude, a sliding vertical window with a width of 20 km was used to calculate the power spectrum by using Welch's averaged periodogram [*Welch*, 1967]. The window was shifted every 1 km. The power spectra from all profiles of the night were then averaged. This power spectrum represents the temperature variance versus vertical wave number. To represent the true wave energy variation with altitude, we need to scale the power spectra to be proportional to the wave potential energy, which is defined as

$$E_{pv}(z) = \frac{\rho_0(z)}{2} \frac{g^2}{N^2(z)} \overline{\left(\frac{T'(z)}{T_0(z)}\right)^2}, \tag{4}$$

where $E_{pv}(z)$ denotes the potential energy per unit volume and $N(z)$ denotes the time averaged Brunt-Väisälä frequency. The wave potential energy is thus proportional to the variance of relative temperature perturbations, the density profile $\rho_0(z)$ and the inverse of $N^2(z)$. Therefore we scaled the power spectra according to equation (4), by dividing a N^2. Here N^2 is calculated as

$$N^2 = \frac{g}{T}\left(\frac{\partial T}{\partial z} + \frac{g}{C_p}\right), \tag{5}$$

where g is the gravity acceleration, c_p is the specific heat at constant pressure, for each temperature profile and then averaged over the night. A fourth-order polynomial was fitted to the nightly mean profile to obtain a smoothed N^2. The effect of $\rho_0(z)$ is also considered by multiplying the spectra with an exponential term $\exp(-z/H_0)$, where H_0 = 7 km. This scaled power spectra should be approximately constant with altitude for nondissipating waves and decrease with altitude when there is an energy loss. Details about the scaled power spectra will be further discussed in section 3.2.

3. Observations and Results

3.1. Background and Perturbations

[10] Temperature measurements by Na lidar and Rayleigh lidar are shown in Figure 1. The highest temperature of ~270 K is observed in the stratopause region. A prominent inversion layer associated with the diurnal tide is present between ~90 and ~100 km. The center of the inversion layer descends from ~96 km at 0800 UT to ~91 km at 1300 UT. The phase speed of downward progression of the inversion layer is about 0.28 m/s. The downward phase progression is much more noticeable at higher altitudes. The phase speed of the downward progression was consistent with that of an upward propagating diurnal tides [*Li et al.*, 2005b]. At higher altitudes, tidal oscillations are much stronger. In the following analysis, tidal oscillations are removed to obtain gravity wave perturbations.

[11] Figure 2 shows the nightly mean temperature profiles from the lidar measurements and two reference atmospheres, CIRA86 [*Fleming et al.*, 1988] and MSIS00 models [*Picone et al.*, 2002]. The nightly mean temperature observed by the Rayleigh lidar shows that the stratopause is located at ~51 km, with a maximum temperature of ~266.4 K. The structure of the upper mesosphere and lower thermosphere observed by Na lidar is more complicated. Two prominent temperature minima are present at ~86 and 100 km, respectively. This "double mesopause," while not in the reference atmospheres, was also observed over Tenerife (28°N) [*Fricke-Begemann et al.*, 2002] and Fort Collins (41°N) [*Yu and She*, 1995]. The best match between measurements and reference atmospheres is between ~50 and ~66 km. Above ~66 km, their differences increase

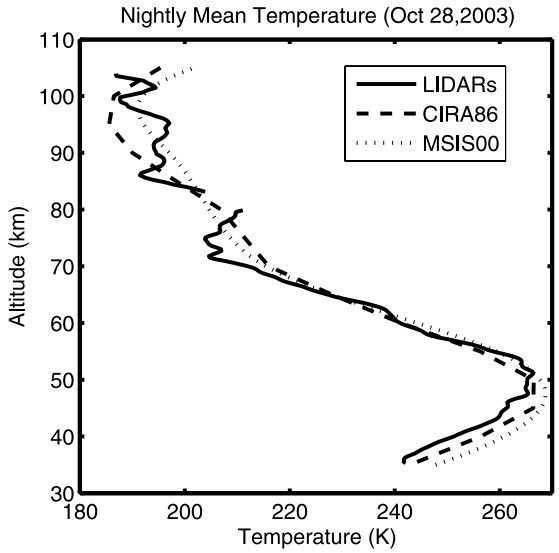

Figure 2. Mean temperature profile obtained from 0519 to 1513 UT, 28 October 2003. The solid lines show the lidar observations over Maui and Mauna Loa; the dashed line and the dotted line represent the CIRA86 and MSIS00 reference atmospheres, respectively.

significantly and vary with altitude; below ~50 km, observed temperatures are lower than both reference atmospheres. *Sharma et al.* [2006] compared the monthly mean temperature profiles with CIRA86 and MSIS00 models over tropic and subtropic stations and had similar findings. The higher temperatures of CIRA86 model below the stratopause were also reported by *McDonald et al.* [1998] with Rayleigh and MST lidar measurements at Aberystwyth (52.4°N, 4.1°W) in Wales.

[12] Na lidar also provides nighttime horizontal wind measurements, as shown by Figure 3. The downward phase progression is more obvious in the meridional wind than in the zonal wind. There was a strong vertical shear of zonal wind between 87 and 90 km before 1200 UT, which gave rise to the dynamic instability and ripple structures [*Li et al.*, 2005b]. Around 95 km, strong northward winds persisted for almost the entire night, which can result in a prominent Doppler shift for northward propagating waves.

[13] Figure 4a shows the relative temperature perturbations from 35 to 103 km, with a gap between 76 and 84 km. Figure 4b shows their standard deviations and measurement uncertainties. The data were smoothed using running average with 1-h and 2.5-km windows in time and altitude, respectively. In Figure 4a, the most significant feature is that a coherent wave structure was observed in both Rayleigh lidar and Na lidar temperatures. The phase fronts of the wave are highlighted by black dotted lines along negative phases of perturbations. The downward phase progression indicates the presence of an upward propagating wave. This dominant wave mode lasted for the entire night. The vertical wavelength is about 10 km. This result is comparable to the observations of *Rauthe et al.* [2006] and *Sica and Russell* [1999], who found that only a few dominant wave components

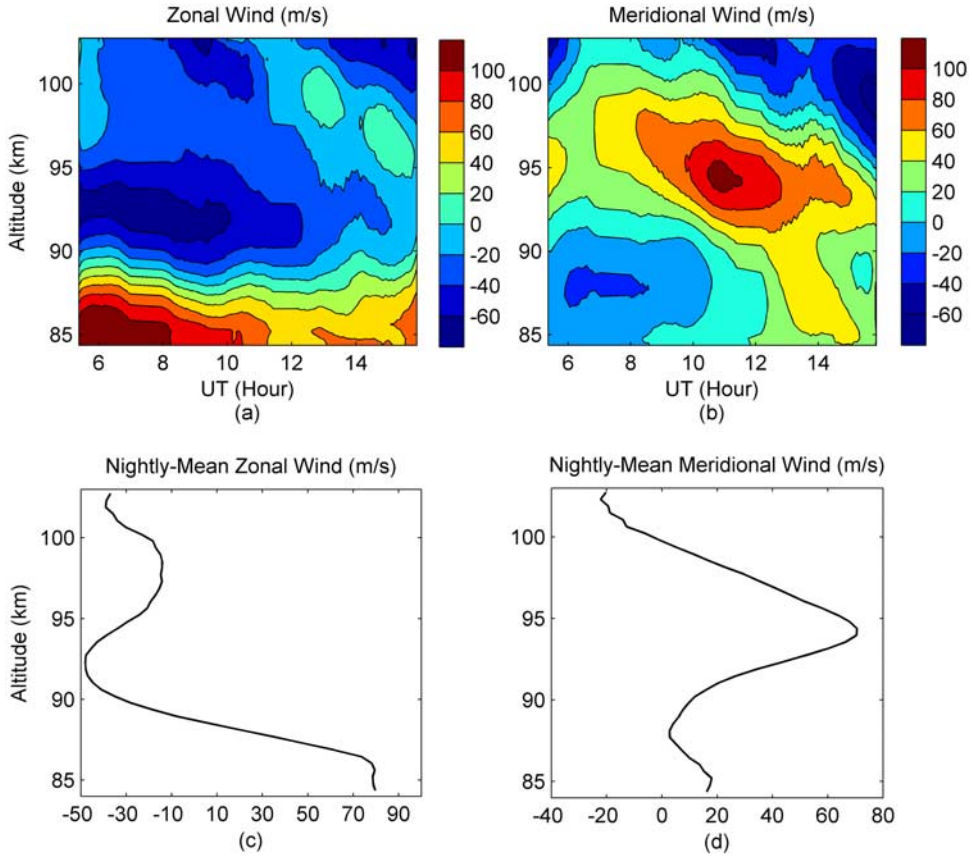

Figure 3. (a) Zonal and (b) meridional winds on the night of 28 October 2003. Nightly mean (c) zonal and (d) meridional winds.

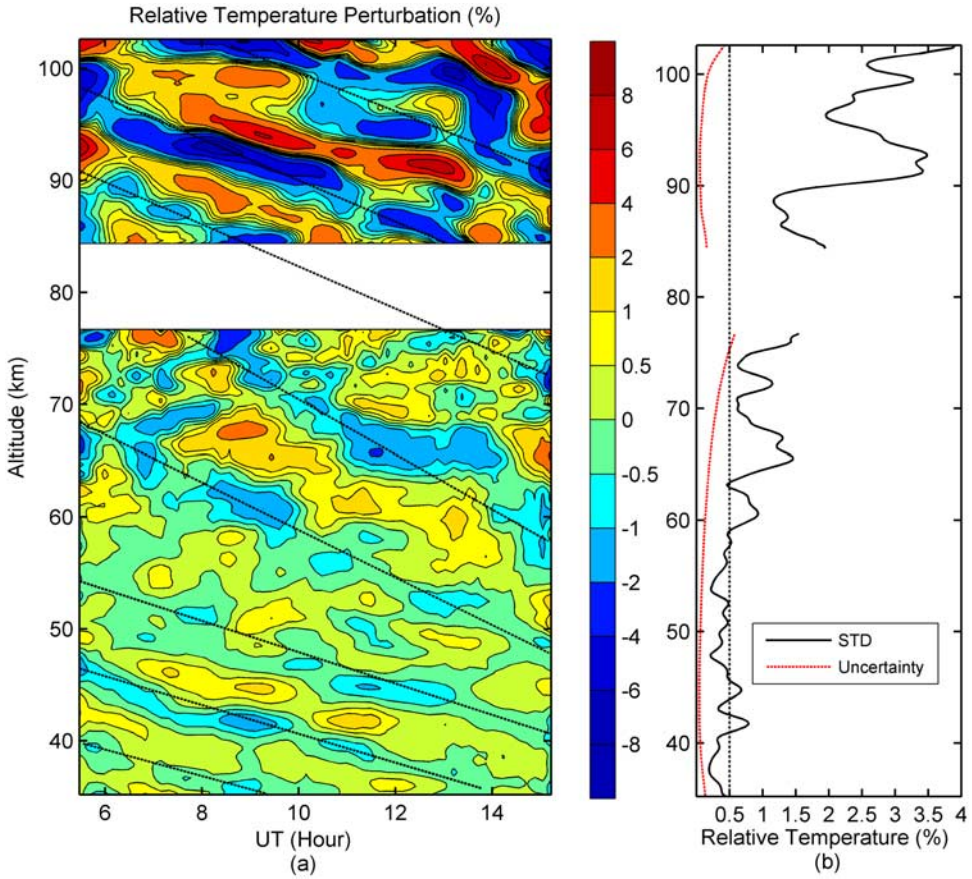

Figure 4. (a) Smoothed relative temperature perturbations after removing tides and high-frequency perturbations on the night of 28 October 2003. Black dotted lines indicate the downward phase progressions. (b) The standard deviation of relative temperature perturbations over the night (solid black line) and its statistical uncertainty (dotted red line).

exist in such observations. Since the wave perturbations have similar structures throughout the altitude and the phase progression lines can be connected through the gap region, it suggests that they were originated from the same wave packet and representing the same wave mode. The following discussions are based on our premises that perturbations observed at all levels are from the same wave packet throughout the night and the wave's horizontal scale is large compared to the distance between the two observation sites. Therefore the difference from the two sites due to horizontal variation of the wavefield can be ignored. These premises will be affirmed in section 3.3.

[14] A distinct dominant GW mode with long period (several hours) and large vertical wavelength (tens of kilometers) that was similar to our findings was also found in the stratosphere and lower mesosphere (~35–60 km), as studied by *Wilson et al.* [1991]. Besides, according to lidar observation over a low-latitude site (Gadanki, 13.5°N), it was found that the dominant perturbations seen at lower heights (<50 km) with low rates of downward phase progression were due to large vertical wavelength and long-period GWs [*Sivakumar et al.*, 2006]. By analyzing the meteor radar winds at MLT region and Rayleigh composite night temperatures (not shown), we believe that the observed dominate mode of vertical wavelength is likely due to a GW because the vertical wavelengths of the migrating diurnal tide were much longer and determined to be ~25 km in the stratosphere and lower mesosphere and greater than 30 km in MLT region. Semidiurnal tide has even longer wavelength.

[15] Figure 4b shows that the standard deviations of the relative temperature perturbations generally increase with altitude, indicating amplitude growth. The standard deviations are much larger by both Na and Rayleigh observations than the measurement uncertainties, so the dominant wave structures are due to a real geophysical variability and the dominant GW mode observed simultaneously by both lidars is a robust feature. The same smoothing was applied to the Na lidar horizontal winds which are shown in Figure 5. Wind uncertainties vary with the altitude but are all less than 0.8 m/s, much smaller than the perturbation magnitude. Similar to the relative temperature perturbations, wind perturbations also show an upward propagating GW structure with vertical wavelength of ~10 km. The zonal and meridional winds were used to derive intrinsic wave properties by the hodograph method discussed in section 2.2 and the results will be shown in section 3.3.

3.2. Wave Propagation and Damping

[16] As shown in Figure 4a, the amplitude of relative temperature perturbations increases almost all the way up from the stratosphere to the lower thermosphere, except for

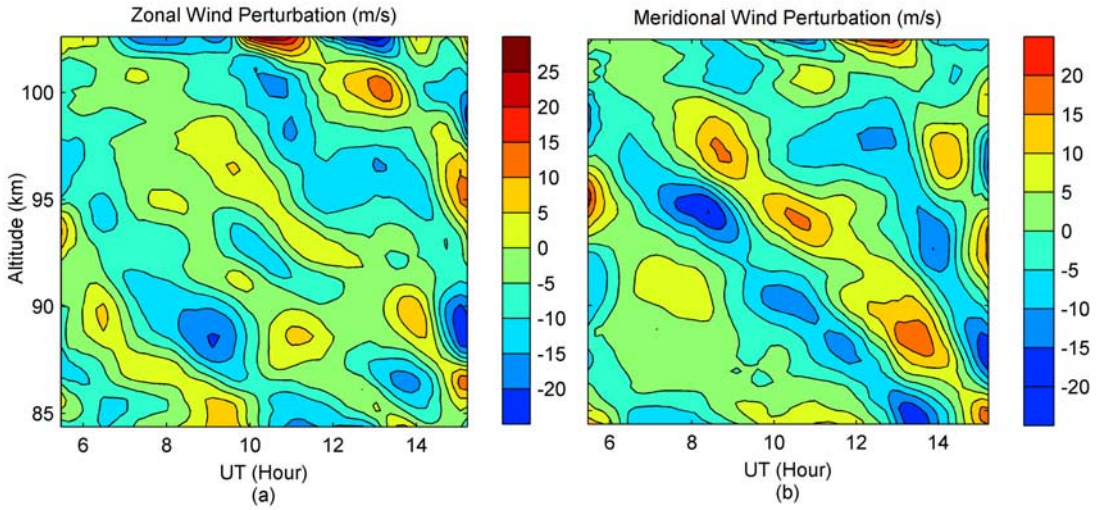

Figure 5. Smoothed (a) zonal and (b) meridional wind perturbations from Na lidar after removing tides and high-frequency perturbations.

the region around stratopause where the wave structure seems to be partly disrupted. Figure 6 shows all temperature perturbation profiles together with the standard deviation (yellow line) and measurement uncertainties (white line). The standard deviation profile is also fitted with an exponential function defined as

$$f\left(\frac{\Delta T}{\bar{T}}\right) = a \exp\frac{z - z_0}{2H}, \tag{6}$$

where a denotes the amplitude roughly at the height z_0(z_0 = 35.2 km) and H denotes the scale height. The fitting results are

$$\begin{matrix} a = (0.26 \pm 0.04)\ (\%) \\ H = 14 \pm 1\ (\text{km}) \end{matrix}. \tag{7}$$

This is shown as the red line in Figure 6. A green line with a scale height of 7 km is also shown, which indicates the amplitude growth of a freely propagating GW. They have the same amplitudes at the starting point z_0 = 35.2 km. The substantial discrepancy between the red and green lines indicates that the waves were not freely propagating and the observed GWs were partially dissipated.

[17] It is noticed that the vertical fluctuation profile has a wavy structure, which means that fluctuations do not always increase with the altitude. Instead, at some altitudes, minima and maxima fluctuations are frequently observed. For instance, as shown in Figure 6, there are several minimum values located at ~43, 48, 54, 63 and 70 km in the lower layer, and at ~89 and 96 km in the upper layer. The altitudes with minimal fluctuations were also observed and referred to as "nodes" by *Rauthe et al.* [2006]. Between 46 and 58 km, the fluctuations are smallest, all less than

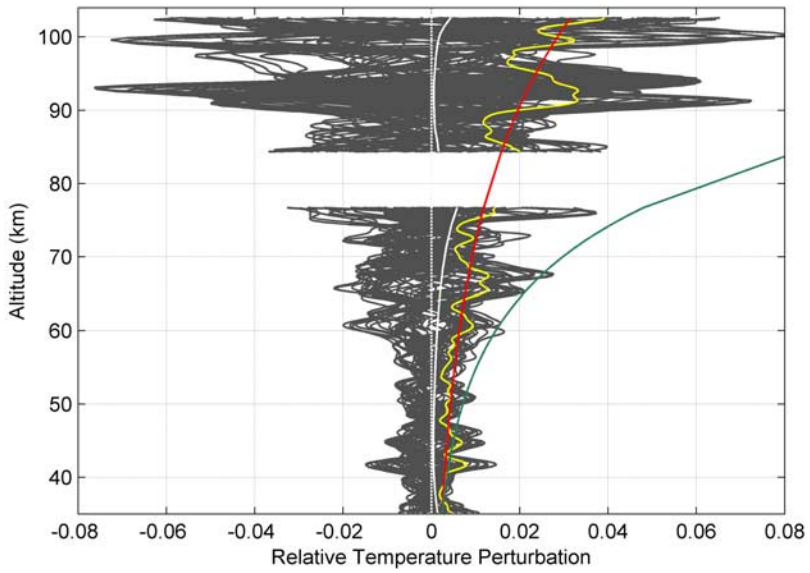

Figure 6. Individual relative temperature perturbation profiles (gray), standard deviation (yellow), and measurement uncertainty (white). The red line is an exponential fit to the standard deviation, and the green line indicates the exponential increase of a freely propagating GW with a scale height of 7 km.

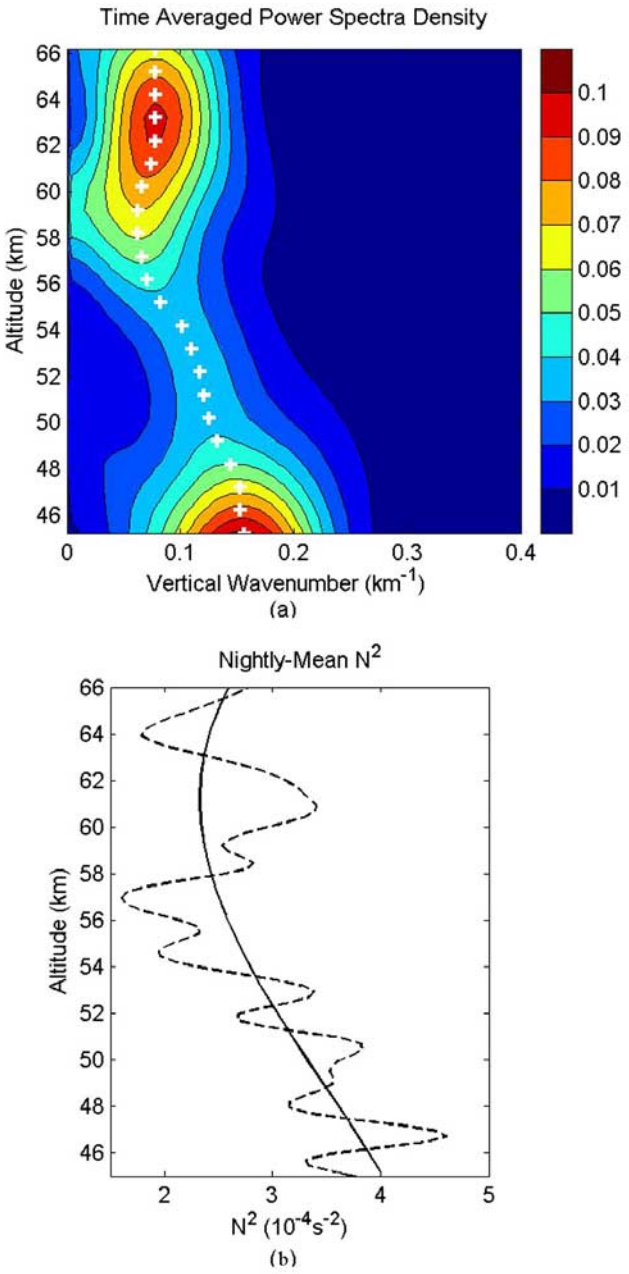

Figure 7. (a) Power spectral density proportional to GW potential energy. Unit is arbitrary. The white crosses indicate wave numbers where power is at maximum. (b) Nightly mean N^2 (dashed line) and its fourth-order polynomial fit (solid line).

0.5%. This suggests that waves may have experienced severe dissipation in this region. In addition, Figure 4a also shows that the "disrupted layer" starts at ~58 km early in the night and then descends to ~46 km toward the end of the night. We will refer to this layer as the "damping layer" hereinafter. It appears that the wave experienced strong dissipation as it propagated through the damping layer but then reappeared above it. Generally, the center of the damping layer descends with time and its thickness has the scale of about one vertical wavelength.

[18] It is particularly named not only because within the damping layer, wave fluctuations are small (less than 0.5%) and not increasing with the altitude, but also because it is linked with the transition of the vertical wavelength, as the scaled power spectra of vertical wave number shows in Figure 7a. As we discussed in section 2.2, the scaled power spectra for all profiles of the night were calculated and then averaged for the entire night. Figure 7a shows the mean scaled power spectra of relative temperature perturbations from 45 to 66 km. It represents the GW energy variation as a function of vertical wave number and altitude. The white cross in Figure 7a indicates the wave number where the PSD is maximum at each altitude. Figure 7b shows the nightly mean N^2 as a function of altitude. Its fourth-order polynomial fitting is represented by the black solid line.

[19] A prominent feature of the spectra is that the wave energy decreases from 45 km up and reaches minimum values between 49 and 55 km. Above 55 km, the wave energy increases again. The significant damping occurs around the stratopause, where a gradual increase of the dominant vertical wavelength is also observed. The dominant vertical wavelength increases from ~6–7 km at 45 km to ~12–13 km at 66 km.

[20] The wave dispersion relation described by equation (3) can be rewritten as

$$m^2 = \frac{k^2N^2}{\omega^2 - f^2} = \frac{N^2}{\omega^2/k^2 - f^2/k^2} = \frac{N^2}{|c-U|^2 - f^2/k^2}, \quad (8)$$

where c is the ground-based horizontal phase speed and U is the background wind speed in the direction of wave propagation. It shows that the vertical wavelength can vary with N^2 and the background horizontal wind U. This decrease of the dominant vertical wavenumber is thus consistent with the decrease of N^2 shown in Figure 7b. We note that the vertical wavelength is also sensitive to the background winds. However, we cannot examine the wind effect directly for this case because of lack of wind data below 80 km. On the basis of the Horizontal Wind Model (HWM) [*Hedin et al.*, 1996] at the same time and location as our observations, we found that the zonal wind has the order of 10 m/s and meridional wind starts with 10 m/s at 35 km and can reach roughly 45 m/s near 60 km on this night over Hawaii. This wind background can lead to the change of vertical wavelength on the order of 10 km. It implies that the background wind may also be important to the variation of the vertical wavelength, as found in other studies [*Sato and Yamada*, 1994; *Li et al.*, 2007].

[21] In summary, we observed a dominant GW mode propagating from the stratosphere to the lower thermosphere. A significant damping layer was found around the stratopause region. The dominant vertical wavelength generally increased with altitude below 60 km, which is consistent with the decrease of static stability. In the following section, we will derive wave properties on the basis of a monochromatic GW assumption.

3.3. Wave Properties

[22] Because of the noticeable wavelength change above and below the damping layer, we derive wave properties separately in the stratosphere and mesosphere from Rayleigh

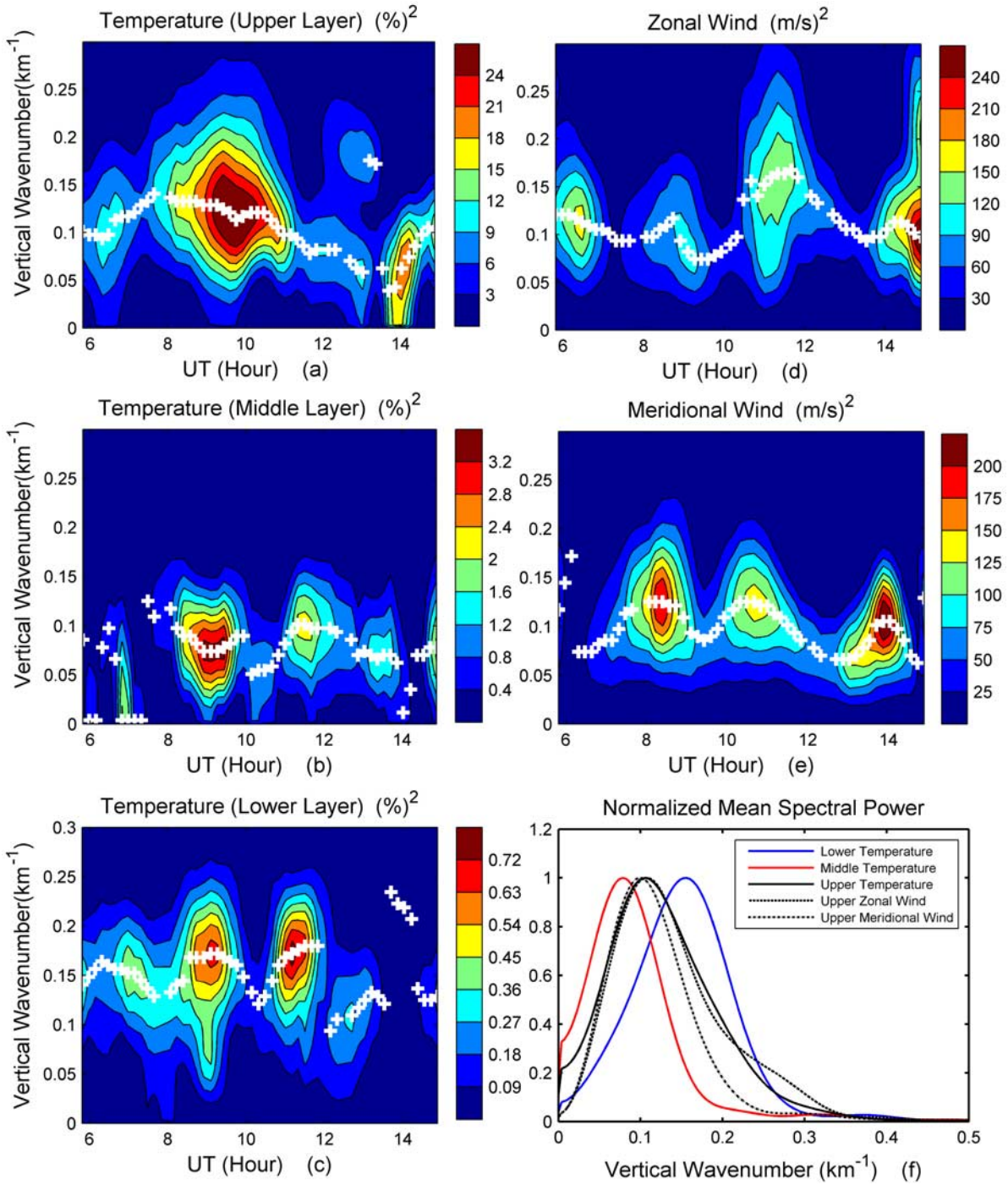

Figure 8. PSDs for relative temperature perturbations in the (a) upper, (b) middle, and (c) lower layers, PSDs for the (d) zonal and (e) meridional perturbations, and (f) the normalized PSDs averaged over the night.

lidar data. We define the "lower layer" from 35 to 55 km and the "middle layer" from 55 to 76 km. The layer observed by Na lidar is referred to as the "upper layer." The spectral analyses were carried out for the three layers by applying the same Welch's periodogram method, with a vertical window of 20 km and shifted every 12 min in time. Figure 8 shows the spectra of relative temperature perturbations in three layers, the spectra of two horizontal wind components, and a normalized total power spectral density for all five quantities. The power spectral density is derived in terms of the square of wave amplitude. Dominant vertical wave numbers are marked by white crosses.

[23] According to Figures 8a–8e, wave intensities show large temporal variations, and they reach maximum at slightly different times for different quantities. On the basis of the PSD of temperature perturbations in the lower layer (Figure 8c), a strong wave occurred between ~0800 and 1000 UT and another one occurred between ~1030 and

Table 1. Maximum and Mean Amplitudes of GWs[a]

Amplitude	Lower Layer Temperature (%)	Middle Layer Temperature (%)	Upper Layer Temperature (%)	Upper Layer Zonal Wind (m/s)	Upper Layer Meridional Wind (m/s)
Maximum	0.9 (2.2 K)	2.0 (4.6 K)	5.4 (10.4 K)	16	15
Mean	0.6 (1.5 K)	1.2 (2.6 K)	3.8 (7.4 K)	10	10

[a]Percentage represents amplitudes of the relative temperature perturbations; the corresponding temperature perturbations are given in parentheses.

1130 UT. The first maximum can be also found in middle and upper layers while the second one become relatively weaker at higher altitudes. The strongest signal in zonal wind is found at the end of the observation period. Three maximum signals are present in the meridional wind, which are centered at ~0830 UT, 1100 UT and 1400 UT. The dominant wavelengths also vary with time in the range of about 6–12 km.

[24] Figure 8f shows the normalized mean PSDs. Red, blue and black solid lines denote the lower, middle and upper layer temperatures while black dashed line represents the zonal wind and dash-dotted line represents the meridional wind in the upper layer. It shows that the mean dominant vertical wavelengths are ~6.4 km and 12.8 km in the lower and middle layers. The dominant vertical wavelengths in upper layer are ~9.5 km, 9.1 km and 10.2 km in temperature, zonal and meridional wind, respectively. Waves with similar vertical wavelengths have also been identified in previous studies [*Chanin and Hauchecorne*, 1981; *Shibata et al.*, 1986; *Hu et al.*, 2002].

[25] Wave amplitude is derived from its corresponding PSD and the mean and maximum values are listed in Table 1. If the wave is freely propagating which means the amplitude will increase with the scale height $2H_s$ as the density decrease exponentially with H_s ($H_s \approx 7$ km), the maximum amplitude in the middle layer would be 3.6% and the upper layer would be 30.9%, which are much larger than the maximum amplitudes observed. The observed maximum amplitudes in the middle and upper layers are 2.2% and 5.4%, respectively (Table 1). It means that the wave was not freely propagating and was dissipating as it propagated upward. The maximum amplitudes of zonal wind and meridional wind were 16 and 15 m/s, respectively.

[26] Since both temperature and wind data were available in the upper layer from the Na lidar measurement, the wave parameters can be derived from hodograph analysis described in section 2.2. Figure 9 is the hodograph of zonal and meridional winds from all the profiles with significant wave amplitudes and common dominant vertical wavelength in both temperature and wind. The wave propagated along the major axis of the hodograph and according to the rotation direction of temperature and in-phase wind perturbations with the altitude, it propagated northward [*Hu et al.*, 2002]. The average intrinsic period is 15 h and the average horizontal wavelength is 2140 km, which is significantly larger than the distance between two lidar observation sites (~150 km). For the two sites, the properties of the dominant mode are similar, which reaffirms our assumption that the wavefield was nearly homogeneous between the two stations for the dominant wave mode.

[27] The ground-based phase speed can also be estimated from the measured wave period. As shown by the temporal spectrum in Figure 10, the wave period varies between 5 and 7 h from the lower to the upper layers with the mean around 6 h. The relation between observed and intrinsic periods is

$$\lambda_h = |c - U|\tau_I = c\tau_O, \tag{9}$$

where τ_I and τ_O are intrinsic and observed (ground-based) periods, respectively and λ_h is horizontal wavelength. Here we use the following values:

$$\lambda_h = 2140\,\text{km}, \tau_I = 15\,\text{h}, \tau_O = 6\,\text{h}, \tag{10}$$

and estimate $c = 99$ m/s and $|c - U| = 40$ m/s. This gives $U = 59$ m/s if the background wind is in the same direction as wave propagates and $U = 139$ m/s if they are opposite. At the altitude where this quasi-6-h wave was strongest (93 km), we can find that the background meridional wind (Figure 3d) is about 60 m/s, matched well with the first solution of U. It again indicates that the wave was propagating northward in this altitude region, which is consistent with the hodograph result.

[28] The vertical phase speeds were also calculated from observed vertical wavelengths and periods. The mean vertical phase speed increases from 0.3 m/s in the lower layer to 0.6 m/s in the middle layer and is 0.44 m/s in the upper layer. Same as the vertical wavelength, the vertical phase speed is also larger in the mesosphere compared to the stratosphere owing to the change of static stability. *Rauthe et al.* [2006] also pointed out that vertical phase velocity was larger in the mesosphere than in the stratosphere

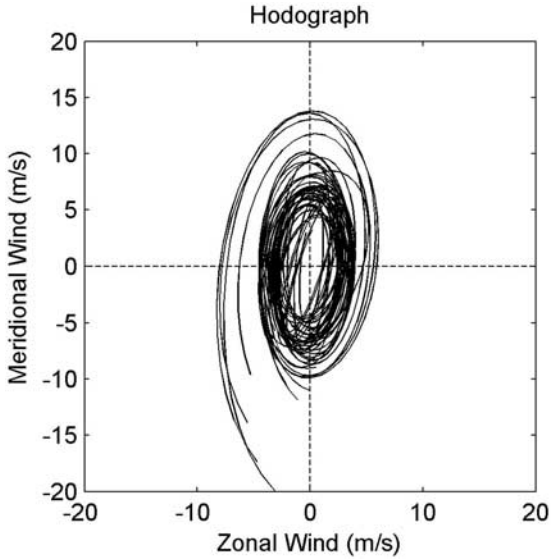

Figure 9. Hodograph of zonal and meridional wind perturbations.

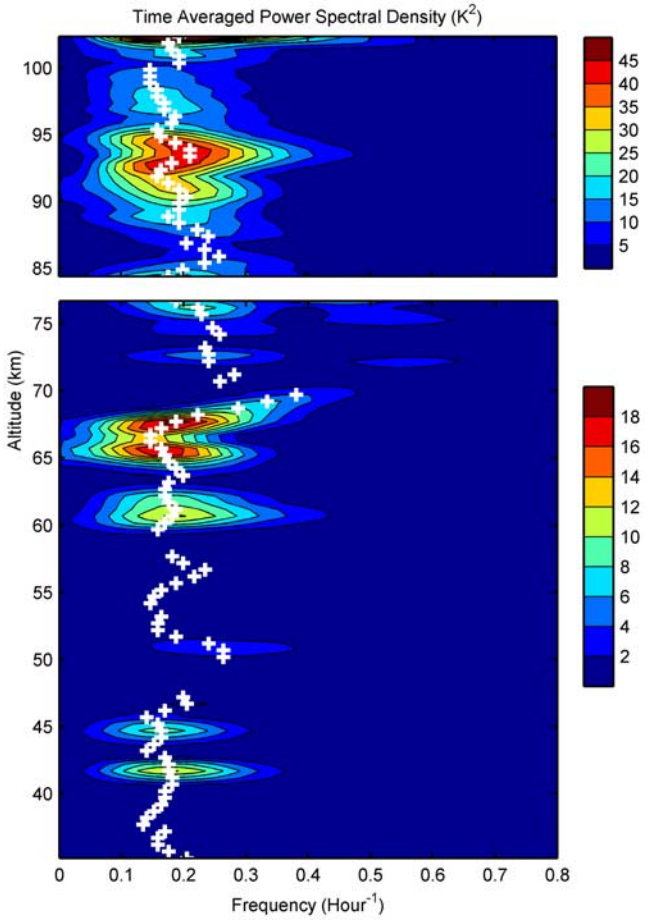

Figure 10. Nightly mean frequency PSD of GW perturbations as a function of altitude. White crosses indicate dominant frequencies at each altitude.

because of the decreasing static stability. In the stratosphere, N is larger compared to the mesosphere which results in smaller vertical wavelengths and smaller vertical phase speeds which is also observed in our analysis.

[29] The values of vertical phase speeds are quite typical compared with previous radar and lidar observations. For instance, *Gardner et al.* [1989] obtained values 0.11 to 0.85 m/s with the mean value of 0.39 m/s in stratosphere using Rayleigh lidar observations. *Sivakumar et al.* [2006] estimated the rate of downward progression of GWs at around 0.15–0.3 m/s for lower heights (<50 km) on the basis of four nights of Rayleigh lidar observations over Gadanki (13.5°N). For the higher altitude, vertical phase speed measured in the Na layer (85–105 km) ranged from 0.36 to 1.75 m/s [*Gardner and Voelz*, 1987]. And the combined lidar temperature measurements of GWs from 1 to 105 km indicated the vertical phase speed ranged from 0.25 to 0.75 m/s in November 2003 [*Rauthe et al.*, 2006]. The variation of the vertical phase speed with altitude was also reported by *Chanin and Hauchecorne* [1981], who showed that the vertical phase velocity was near 1 m/s at 50–70 km and less than 0.2 m/s below 50 km. It is believed that GWs with similar phase speeds were frequently observed in different seasons and at different locations. Weather events, like convective systems and jet streams can excite GWs for the most part of the world, which may be a source for the universally observed GWs [*Fritts and Alexander*, 2003]. It should be noticed that they are different from globally migrating tides, considering the distinctive wave sources.

3.4. Static Stability

[30] Figure 11a shows N^2 as a function of time and altitude, and Figure 11b shows its nightly mean. It is found that there was a persistent low-stability layer between 54 and 58 km for the entire night. Some unstable regions are located mainly above 60 km in the middle layer and some

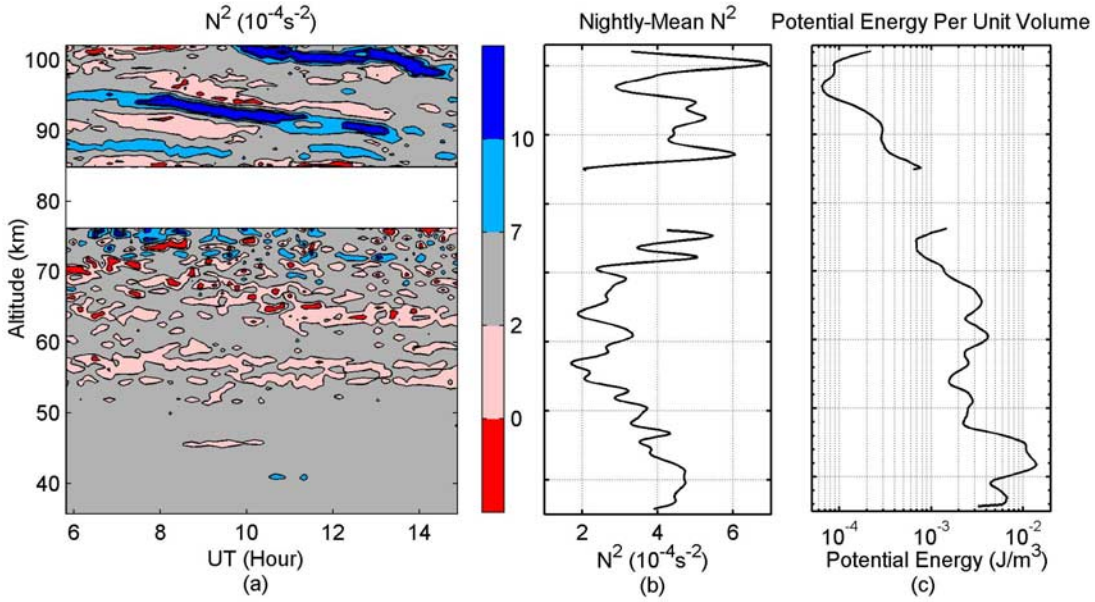

Figure 11. (a) Time-altitude variation of N^2, (b) nightly mean N^2 and (c) potential energy per unit volume. In Figure 11a, red denotes convectively unstable areas and pink denotes marginally stable areas where $0 < N^2 < 2 \times 10^{-4}$ s^{-2}.

are found in the upper layer. Notice that because of lower signal-to-noise ratio, some of the unstable regions above 60 km are likely due to measurement uncertainties [*Zhao et al.*, 2003]. The persistent low-stability layer between 54 and 58 km is more likely to be a robust feature and contributing to the observed damping layer. As wave propagating through this layer, it is more likely to saturate and dissipate. In the upper layer, the unstable regions have a downward phase progression, which is probably caused by the temperature changes associated with the diurnal tides.

[31] Also shown in Figure 11c is the GW's potential energy as defined in equation (6). It is calculated on the basis of the standard deviation shown in Figure 4b and the nightly mean N^2 in Figure 11b. The atmospheric density is obtained from MSIS00 model. It is interesting to note that several local minima of the nightly mean N^2 in Figure 11b all correspond to local minima of the potential energy in Figure 11c. Common local minima are present at ~54, 63, 89 and 96 km. It is implying that the changing static stability imposes a significant influence on the wave propagation and energy dissipation.

4. Discussion and Summary

[32] A low-frequency inertial GW was observed to propagate upward from the stratosphere to the mesosphere from the simultaneous measurements of Rayleigh and Na lidars over Hawaii islands on the night of 28 October 2003. On the basis of the relative temperature perturbations, a persistent wave mode was found. The mean dominant vertical wavelength was ~6.4 km in the lower layer (35–55 km) and ~12.8 km in the middle layer (55–76 km). In the upper layer (84–103 km), the mean dominant vertical wavelength was found to be around 9.6 km from both temperature and wind measurements. The variation of the dominant vertical wavelength was consistent with the variation of background static stability. The scale height of the relative temperature fluctuation with the altitude was ~14 km, implying that GW was dissipating. Maximum wave amplitudes were 2.2, 4.6 and 10.4 K in the lower, middle and upper layers, respectively. A significant damping layer with the wave structure being clearly disrupted was observed above the stratopause, where the static stability was small. Na lidar temperature and horizontal winds were used in hodograph analysis to further determine the wave parameters. It was found that the wave was propagating northward, with an apparent horizontal phase speed of 99 m/s. It had an intrinsic horizontal phase speed of 40 m/s, intrinsic period of 15 h, and horizontal wavelength of 2140 km.

[33] This analysis showed that combined measurements from lower stratosphere to the mesopause region are very useful for the study of GW propagation. The wind data in the MLT region in addition to temperature allowed us to derive wave intrinsic parameters, and revealed that the wave was Doppler shifted by the meridional wind. Wind measurement in the stratosphere and lower mesosphere could further quantify such analysis.

[34] The presence of a low-frequency inertial GW throughout the night is perhaps not uncommon, as it has also been observed in other studies. However, the measurement at single location also proposed some limitations in the interpretation of the observed wave characteristics. In our analysis, the implicit assumption is that the wavefield is horizontally uniform and temporally invariant. This is of course not always true. A varying wave source may contribute to a periodic structure observed at a single location that can be erroneously identified as a wave. If a wave packet is not horizontally homogeneous, it can also produce a vertical wave-like structure as it moves across a single station. While these possibilities cannot be ruled out, the assumptions may be often applicable for our nighttime measurements during clear weather conditions at Hawaii. It is likely that the GW we observed on this night was from a nearly constant wave source south of Hawaii near the equator, where tropical convections are present. In the tropics, where it is less likely to have GW generation from topography and baroclinic instability, the source of inertial gravity waves in the troposphere or the lower stratosphere is most likely tropical convection as has been found in many studies [*Pfister et al.*, 1993; *Tsuda et al.*, 1994; *Karoly et al.*, 1996; *Wada et al.*, 1999; *Vincent and Alexander*, 2000]. Tropical convection provides an important mechanism to excite the inertial GWs as we observed here. The low-frequency waves were usually generated in the lower atmosphere near the convective source and can be observed in the middle atmosphere at large horizontal distance from it [*Fritts and Alexander*, 2003]. For us to observe the inertial GWs over the Hawaii islands, the upward and northward propagation should be present to observe GWs originated from the tropical convection region. The fact that the GW we identified was propagating northward supports this notion.

[35] **Acknowledgments.** We would like to thank NASA Jet Propulsion Laboratory (California Institute of Technology) for providing the Rayleigh lidar observation. This study is sponsored by NSF grants ATM 05-45704, the lidar consortium grant, and ATM 07-37656.

References

Alpers, M., R. Eixmann, C. Fricke-Begemann, M. Gerding, and J. Höffner (2004), Temperature lidar measurements from 1 to 105 km altitude using resonance, Rayleigh, and rotational Raman scattering, *Atmos. Chem. Phys.*, *4*, 793–800.

Bühler, O., and M. E. McIntyre (1999), On shear-generated gravity waves that reach the mesosphere. Part II: Wave propagation, *J. Atmos. Sci.*, *56*(21), 3764–3773, doi:10.1175/1520-0469(1999)056<3764:OSGGWT>2.0.CO;2.

Chanin, M. L., and A. Hauchecorne (1981), Lidar observation of gravity and tidal waves in the stratosphere and mesosphere, *J. Geophys. Res.*, *86*(C10), 9715–9721, doi:10.1029/JC086iC10p09715.

Dao, P. D., R. Farley, X. Tao, and C. S. Gardner (1995), Lidar observations of the temperature profile between 25 and 103 km: Evidence of strong tidal perturbation, *Geophys. Res. Lett.*, *22*(20), 2825–2828, doi:10.1029/95GL02950.

Fleming, E. L., S. Chandra, M. R. Shoeberl, and J. J. Barnett (1988), Monthly mean global climatology of temperature, wind, geopotential height and pressure for 0–120 km, *NASA Tech. Memo.*, *100697*, 85 pp.

Fricke-Begemann, C., J. Höffner, and U. von Zahn (2002), The potassium density and temperature structure in the mesopause region (80–105 km) at a low latitude (28°N), *Geophys. Res. Lett.*, *29*(22), 2067, doi:10.1029/2002GL015578.

Friedman, J. S. (2003), Tropical mesopause climatology over the Arecibo Observatory, *Geophys. Res. Lett.*, *30*(12), 1642, doi:10.1029/2003GL016966.

Fritts, D. C. (1985), A numerical study of gravity-wave saturation—Nonlinear and multiple wave effects, *J. Atmos. Sci.*, *42*(19), 2043–2058, doi:10.1175/1520-0469(1985)042<2043:ANSOGW>2.0.CO;2.

Fritts, D. C., and M. J. Alexander (2003), Gravity wave dynamics and effects in the middle atmosphere, *Rev. Geophys.*, *41*(1), 1003, doi:10.1029/2001RG000106.

Fritts, D. C., and P. K. Rastogi (1985), Convective and dynamical instabilities due to gravity-wave motions in the lower and middle atmosphere:

Theory and observations, *Radio Sci.*, *20*(6), 1247–1277, doi:10.1029/RS020i006p01247.

Fritts, D. C., and L. Yuan (1989), Stability analysis of inertio-gravity-wave structure in the middle atmosphere, *J. Atmos. Sci.*, *46*(12), 1738–1745, doi:10.1175/1520-0469(1989)046<1738:SAOIWS>2.0.CO;2.

Gardner, C. S., and G. C. Papen (1995), Mesospheric Na wind/temperature lidar, *Rev. Laser Eng.*, *23*, 131–134.

Gardner, C. S., and D. G. Voelz (1987), Lidar studies of the nighttime sodium layer over Urbana, Illinois: 2. Gravity waves, *J. Geophys. Res.*, *92*(A5), 4673–4694, doi:10.1029/JA092iA05p04673.

Gardner, C. S., M. S. Miller, and C. H. Liu (1989), Rayleigh lidar observations of gravity-wave activity in the upper-stratosphere at Urbana, Illinois, *J. Atmos. Sci.*, *46*(12), 1838–1854, doi:10.1175/1520-0469(1989)046<1838:RLOOGW>2.0.CO;2.

Gardner, C. S., Y. Zhao, and A. Z. Liu (2002), Atmospheric stability and gravity wave dissipation in the mesopause region, *J. Atmos. Sol. Terr. Phys.*, *64*(8–11), 923–929, doi:10.1016/S1364-6826(02)00047-0.

Gavrilov, N. M., S. Fukao, T. Nakamura, and T. Tsuda (1996), Statistical analysis of gravity waves observed with the middle and upper atmosphere radar in the middle atmosphere: 1. Method and general characteristics, *J. Geophys. Res.*, *101*(D23), 29,511–29,521, doi:10.1029/96JD01447.

Hedin, A. E., et al. (1996), Empirical wind model for the upper, middle and lower atmosphere, *J. Atmos. Terr. Phys.*, *58*, 1421–1447, doi:10.1016/0021-9169(95)00122-0.

Hu, X., A. Z. Liu, C. S. Gardner, and G. R. Swenson (2002), Characteristics of quasi-monochromatic gravity waves observed with Na lidar in the mesopause region at Starfire Optical Range, NM, *Geophys. Res. Lett.*, *29*(24), 2169, doi:10.1029/2002GL014975.

Karoly, D. J., G. L. Roff, and M. J. Reeder (1996), Gravity wave activity associated with tropical convection detected in TOGA COARE sounding data, *Geophys. Res. Lett.*, *23*(3), 261–264, doi:10.1029/96GL00023.

Leblanc, T., I. S. McDermid, A. Hauchecorne, and P. Keckhut (1998), Evaluation of optimization of lidar temperature analysis algorithms using simulated data, *J. Geophys. Res.*, *103*(D6), 6177–6187, doi:10.1029/97JD03494.

Leblanc, T., I. S. McDermid, and D. A. Ortland (1999a), Lidar observations of the middle atmospheric thermal tides and comparison with the High Resolution Doppler Imager and Global-Scale Wave Model: 1. Methodology and winter observations at Table Mountain (34.4°N), *J. Geophys. Res.*, *104*(D10), 11,917–11,929, doi:10.1029/1999JD900007.

Leblanc, T., I. S. McDermid, and D. A. Ortland (1999b), Lidar observations of the middle atmospheric thermal tides and comparison with the High Resolution Doppler Imager and Global Scale Wave Model: 2. October observations at Mauna Loa (19.5°N), *J. Geophys. Res.*, *104*(D10), 11,931–11,938, doi:10.1029/1999JD900008.

Li, F., A. Z. Liu, and G. R. Swenson (2005a), Characteristics of instabilities in the mesopause region over Maui, Hawaii, *J. Geophys. Res.*, *110*, D09S12, doi:10.1029/2004JD005097.

Li, F., A. Z. Liu, G. R. Swenson, J. H. Hecht, and W. A. Robinson (2005b), Observations of gravity wave breakdown into ripples associated with dynamical instabilities, *J. Geophys. Res.*, *110*, D09S11, doi:10.1029/2004JD004849.

Li, T., C.-Y. She, H.-L. Liu, T. Leblanc, and I. S. McDermid (2007), Sodium lidar–observed strong inertia-gravity wave activities in the mesopause region over Fort Collins, Colorado (41°N, 105°W), *J. Geophys. Res.*, *112*, D22104, doi:10.1029/2007JD008681.

Li, T., T. Leblanc, and I. S. McDermid (2008), Interannual variations of middle atmospheric temperature as measured by the JPL lidar at Mauna Loa Observatory, Hawaii (19.5°N, 155.6°W), *J. Geophys. Res.*, *113*, D14109, doi:10.1029/2007JD009764.

Lindzen, R. S. (1981), Turbulence and stress owing to gravity-wave and tidal breakdown, *J. Geophys. Res.*, *86*(C10), 9707–9714, doi:10.1029/JC086iC10p09707.

Lintelman, S. A., and C. S. Gardner (1994), Observation and interpretation of spectra of atmospheric gravity wave perturbations with upward and downward phase progression, *J. Geophys. Res.*, *99*(D8), 16,959–16,971, doi:10.1029/94JD01118.

Liu, A. Z., and C. S. Gardner (2004), Vertical dynamical transport of mesospheric constituents by dissipating gravity waves, *J. Atmos. Sol. Terr. Phys.*, *66*, 267–275, doi:10.1016/j.jastp.2003.11.002.

Liu, A. Z., and C. S. Gardner (2005), Vertical heat and constituent transport in the mesopause region by dissipating gravity waves at Maui, Hawaii (20.7°N), and Starfire Optical Range, New Mexico (35°N), *J. Geophys. Res.*, *110*, D09S13, doi:10.1029/2004JD004965.

Liu, A. Z., R. G. Roble, J. H. Hecht, M. F. Larsen, and C. S. Gardner (2004), Unstable layers in the mesopause region observed with Na lidar during the Turbulent Oxygen Mixing Experiment (TOMEX) campaign, *J. Geophys. Res.*, *109*, D02S02, doi:10.1029/2002JD003056.

Lombard, P. N., and J. J. Riley (1996), Instability and breakdown of internal gravity waves. 1. Linear stability analysis, *Phys. Fluids*, *8*(12), 3271–3287, doi:10.1063/1.869117.

Manson, A. H., and C. E. Meek (1988), Gravity wave propagation characteristics (60–120 km) as determined by the Saskatoon MF Radar (Gravnet) System: 1983–85 at 52°N, 107°W, *J. Atmos. Sci.*, *45*(6), 932–946, doi:10.1175/1520-0469(1988)045<0932:GWPCKA>2.0.CO;2.

McDermid, I. S., T. D. Walsh, A. Deslis, and M. L. White (1995), Optical systems design for a stratospheric lidar system, *Appl. Opt.*, *34*, 6201–6210, doi:10.1364/AO.34.006201.

McDonald, A. J., L. Thomas, and D. P. Wareing (1998), Night-to-night changes in the characteristics of gravity waves at stratospheric and lower-mesospheric heights, *Ann. Geophys.*, *16*, 229–237, doi:10.1007/s00585-998-0229-0.

Murayama, Y., T. Tsuda, R. Wilson, H. Nakane, S. A. Hayashida, N. Sugimoto, I. Matsui, and Y. Sasano (1994), Gravity wave activity in the upper stratosphere and lower mesosphere observed with the Rayleigh lidar at Tsukuba, Japan, *Geophys. Res. Lett.*, *21*(14), 1539–1542, doi:10.1029/93GL02693.

Pfister, L., S. Scott, M. Loewenstein, S. Bowen, and M. Legg (1993), Mesoscale disturbances in the tropical stratosphere excited by convection: Observations and effects on the stratospheric momentum budget, *J. Atmos. Sci.*, *50*(8), 1058–1075, doi:10.1175/1520-0469(1993)050<1058:MDITTS>2.0.CO;2.

Picone, J. M., A. E. Hedin, D. P. Drob, and A. C. Aikin (2002), NRLMSISE-00 empirical model of the atmosphere: Statistical comparisons and scientific issues, *J. Geophys. Res.*, *107*(A12), 1468, doi:10.1029/2002JA009430.

Rauthe, M., M. Gerding, J. Höffner, and F. J. Lübken (2006), Lidar temperature measurements of gravity waves over Kuhlungsborn (54°N) from 1 to 105 km: A winter-summer comparison, *J. Geophys. Res.*, *111*, D24108, doi:10.1029/2006JD007354.

Sato, K., and M. Yamada (1994), Vertical structure of atmospheric gravity waves revealed by the wavelet analysis, *J. Geophys. Res.*, *99*(D10), 20,623–20,631, doi:10.1029/94JD01818.

Serafimovich, A., P. Hoffmann, D. Peters, and V. Lehmann (2005), Investigation of inertia-gravity waves in the upper troposphere/lower stratosphere over northern Germany observed with collocated VHF/UHF radars, *Atmos. Chem. Phys.*, *5*, 295–310.

Sharma, S., V. Sivakumar, H. Bencherif, H. Chandra, Y. B. Acharya, A. Jayaraman, P. B. Rao, and D. N. Rao (2006), A comprehensive study on middle atmospheric thermal structure over a tropic and sub-tropic stations, *Adv. Space Res.*, *37*, 2278–2283, doi:10.1016/j.asr.2005.09.003.

She, C. Y., J. R. Yu, D. A. Krueger, R. Roble, P. Keckhut, A. Hauchecorne, and M.-L. Chanin (1995), Vertical structure of the midlatitude temperature from stratosphere to mesopause (30–105 km), *Geophys. Res. Lett.*, *22*(4), 377–380, doi:10.1029/95GL00010.

Shibata, T., T. Fukuda, and M. Maeda (1986), Density fluctuations in the middle atmosphere over Fukuoka observed by an XeF Rayleigh lidar, *Geophys. Res. Lett.*, *13*(11), 1121–1124, doi:10.1029/GL013i011p01121.

Sica, R. J., and A. T. Russell (1999), How many waves are in the gravity wave spectrum?, *Geophys. Res. Lett.*, *26*(24), 3617–3620, doi:10.1029/1999GL003683.

Sivakumar, V., P. B. Rao, and H. Bencherif (2006), Lidar observations of middle atmospheric gravity wave activity over a low-latitude site (Gadanki, 13.5°N, 79.2°E), *Ann. Geophys.*, *24*, 823–834.

Smith, S. M., M. Mendillo, J. Baumgardner, and R. R. Clark (2000), Mesospheric gravity wave imaging at a subauroral site: First results from Millstone Hill, *J. Geophys. Res.*, *105*(A12), 27,119–27,130, doi:10.1029/1999JA000343.

Swenson, G. R., A. Z. Liu, F. Li, and J. Tang (2003), High frequency atmospheric gravity wave damping in the mesosphere, *Adv. Space Res.*, *32*, 785–793, doi:10.1016/S0273-1177(03)00399-5.

Tang, J., A. Z. Liu, and G. R. Swenson (2002), High frequency gravity waves observed in OH airglow at Starfire Optical Range, NM: Seasonal variations in momentum flux, *Geophys. Res. Lett.*, *29*(20), 1966, doi:10.1029/2002GL015794.

Taylor, M. J., D. N. Turnbull, and R. P. Lowe (1995), Spectrometric and imaging measurements of a spectacular gravity wave event observed during the ALOHA-93 campaign, *Geophys. Res. Lett.*, *22*(20), 2849–2852, doi:10.1029/95GL02948.

Tsuda, T., Y. Murayama, H. Wiryosumarto, S. W. B. Harijono, and S. Kato (1994), Radiosonde observations of equatorial atmosphere dynamics over Indonesia: 2. Characteristics of gravity waves, *J. Geophys. Res.*, *99*(D5), 10,507–10,516, doi:10.1029/94JD00354.

Vincent, R. A., and M. J. Alexander (2000), Gravity waves in the tropical lower stratosphere: An observational study of seasonal and interannual variability, *J. Geophys. Res.*, *105*(D14), 17,971–17,982, doi:10.1029/2000JD900196.

Wada, K., T. Nitta, and K. Sato (1999), Equatorial inertia-gravity waves in the lower stratosphere revealed by TOGA-COARE IOP data, *J. Meteorol. Soc. Jpn.*, *77*, 721–736.

Welch, P. D. (1967), The use of fast Fourier transform for the estimation of power spectra: A method based on time averaging over short, modified periodograms, *IEEE Trans. Audio Electroacoust.*, *15*, 70–73, doi:10.1109/TAU.1967.1161901.

Whiteway, J. A., and A. I. Carswell (1995), Lidar observations of gravity wave activity in the upper stratosphere over Toronto, *J. Geophys. Res.*, *100*(D7), 14,113–14,124, doi:10.1029/95JD00511.

Wilson, R., M. L. Chanin, and A. Hauchecorne (1991), Gravity waves in the middle atmosphere observed by Rayleigh lidar: 1. Case studies, *J. Geophys. Res.*, *96*(D3), 5153–5167, doi:10.1029/90JD02231.

Yeh, K. C., and C. H. Liu (1981), The instability of atmospheric gravity waves through wave-wave interactions, *J. Geophys. Res.*, *86*(C10), 9722–9728, doi:10.1029/JC086iC10p09722.

Yu, J. R., and C. Y. She (1995), Climatology of a midlatitude mesopause region observed by a lidar at Fort Collins, Colorado (40.6°N, 105°W), *J. Geophys. Res.*, *100*(D4), 7441–7452, doi:10.1029/94JD03109.

Zhao, Y., A. Z. Liu, and C. S. Gardner (2003), Measurements of atmospheric stability in the mesopause region at Starfire Optical Range, NM, *J. Atmos. Sol. Terr. Phys.*, *65*(2), 219–232, doi:10.1016/S1364-6826(02)00288-2.

T. Leblanc and I. S. McDermid, Table Mountain Facility, Jet Propulsion Laboratory, California Institute of Technology, 24490 Table Mountain Road, Wrightwood, CA 92397-0367, USA.

T. Li, School of Earth and Space Sciences, University of Science and Technology of China, 96 JinZhai Road, Hefei, Anhui 230026, China.

A. Z. Liu and G. R. Swenson, Department of Electrical and Computer Engineering, University of Illinois at Urbana-Champaign, 1308 West Main Street, Urbana, IL 61801, USA.

X. Lu, Department of Atmospheric Sciences, University of Illinois at Urbana-Champaign, 105 South Gregory Street, Urbana, IL 61801, USA. (xianlu2@uiuc.edu)